Springer

KSME

Journal of Mechanical Science and Technology 31 (1) (2017) 261~267
www.springerlink.com/content/1738-494x(Print)/1976-3824(Online)
DOI 10.1007/s12206-016-1228-9

Numerical study on a single bladed vertical axis wind turbine under dynamic stall †

Galih Bangga[1,2,*], Go Hutomo[2,3], Raditya Wiranegara[4] and Herman Sasongko[2]

[1]*Institute of Aerodynamics and Gas Dynamics, University of Stuttgart, Pfaffenwaldring 21, 70569 Stuttgart, Germany*
[2]*Mechanical Engineering Department, Institut Teknologi Sepuluh Nopember, Arief Rahman Hakim Street, 60111 Surabaya, Indonesia*
[3]*Tiara Vibrasindo Pratama, Ltd., Penjernihan Street 2, 10210 Jakarta, Indonesia*
[4]*School of Mechanical Aerospace and Civil Engineering, University of Manchester, Oxford Road, M13 9PL Manchester, United Kingdom*

(Manuscript Received May 25, 2016; Revised August 3, 2016; Accepted August 24, 2016)

Abstract

The aim of this study is to investigate the flow development of a single bladed vertical axis wind turbine using Computational fluid dynamics (CFD) methods. The blade is constructed using the NACA 0012 profile and is operating under stalled conditions at tip speed ratio of 2. Two dimensional simulations are performed using a commercial CFD package, ANSYS Fluent 15.0, employing the Menter-*SST* turbulence model. For the preliminary study, simulations of the NACA 0012 airfoil under static conditions are carried out and compared with available measurement data and calculations using the boundary layer code XFOIL. The CFD results under the dynamic case are presented and the resulting aerodynamic forces are evaluated. The turbine is observed to generate negative power at certain azimuth angles which can be divided into three main zones. The blade vortex interaction is observed to strongly influence the flow behavior near the blade and contributes to the power production loss. However, the impact is considered small since it covers only 6.4 % of the azimuth angle range where the power is negative compared to the dynamic stall impact which covers almost 22 % of the azimuth angle range.

Keywords: Aerodynamics; Blade vortex interaction; CFD; Darrieus turbine; Dynamic stall; Flow separation; VAWT

1. Introduction

Wind energy has been identified as one of the most promising sources for renewable energy industry. Two categories of modern wind turbines, namely Horizontal-axis (HAWTs) and Vertical-axis wind turbines (VAWTs), are continuously developed. Nowadays, there is a strong interest from the wind energy community to harvest the energy within built environments at urban, sub-urban and remote areas in addition to large wind farms. HAWTs are not economically and socially suitable for such environments as they need large space to build. Technically, sophisticated yaw mechanism is required because the wind direction often changes significantly. On the other hand, VAWTs have the advantages of a simpler design, lower cost and operability even under the winds with high instability in terms of intensity and direction [1].

It is well known that vertical axis wind turbines exhibit very complex unsteady aerodynamics [1, 2]. The cyclic motion of the blade induces a large variation in the angle of attack (α) even under uniform inflow conditions. In consequence, the aerodynamic loading fluctuates and this can manifest as Dynamic stall (DS) [3]. DS is a phenomenon involving a series of flow separations and reattachments occurring on any lifting surfaces subjected to a rapid unsteady motion [4]. The phenomenon is still not well understood despite its importance to the performance and the stable operation range of wind turbines. DS is initiated by the leading edge separation which leads to the instance of Leading edge vortex (LEV). LEV is convected towards the trailing edge inducing the lift to increase significantly. Close to the trailing edge, Trailing edge vortex (TEV) is formed while the LEV detaches from the blade surface indicating the onset of the stall. This results in a dramatic decrease of the lift coefficient (*Cl*) and a sudden increase of the pitching moment coefficient (*Cm*). The stall inception could then lead to a violent flutter causing a harmful impact to the blade structure.

The Computational fluid dynamics (CFD) approaches have been utilized to study the onset of DS. Wang et al. [5, 6] examined the DS on two-dimensional (2D) oscillating airfoils. They demonstrated that the *SST k-ω* turbulence model [7] gives better predictions compared to the Wilcox *k-ω* [8]. Bangga and Sasongko [9] showed that the DS characteristics were dependent on α range and reduced frequency (f_r). By subsequently adjusting the turbulence viscosity of the *k-ε* turbulence model, Bangga [10] demonstrated that the accuracy of DS simulations at low Reynolds number could be improved. Buchner et al. [11] obtained a good agreement between

*Corresponding author. Tel.: +49 71168563477, Fax.: +49 71168563438
E-mail address: bangga@iag.uni-stuttgart.de
† Recommended by Associate Editor Donghyun You

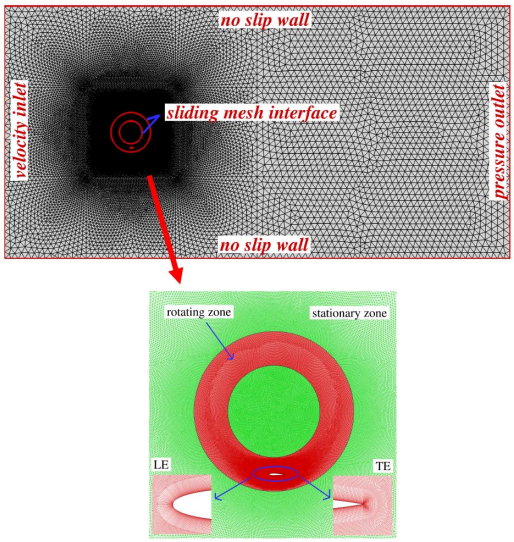

Fig. 1. The computational grid used in the simulations.

URANS simulations and PIV measurements, encouraging the use of CFD to predict the complex behavior of VAWT.

Due to its complexity, Blade-vortex interaction (BVI) is considered as one of the most crucial problems in the numerical modeling of VAWT. Ferreira [12] demonstrated that the BVI contributes to the complex behavior of the resulting forces. Similar studies performed recently by Orlandi et al. [13] using the 3D URANS analysis on a vertical axis wind turbine under skewed flow. They demonstrated that the shed vortices could influence the aerodynamic forces within the wake region. For the time being, discussions related to the BVI are not well explored. Furthermore, the quantifications of losses by the BVI and DS were not well examined. Thus, further studies are necessary.

This paper aims to gain more insights into the DS and the BVI effects on VAWT using CFD. Emphasize is, however, given to the BVI effect which distinguishes the difference with previous publication by Hutomo et al. [4]. In this paper, the quantified effects of DS and BVI are presented. A single bladed Darrieus-type wind turbine was chosen as the model. The rotor radius (R) was 1.2 m. The study was limited to one blade to isolate the development of the complex wake behavior shedding from the multiple blades. The blade was constructed using the NACA 0012 airfoil with the chord length (c) of 0.15 m and the pitch angle of 0°.

2. Computational setup

The hybrid mesh technique was employed in this study, combining the structured mesh in the vicinity of the blade surface to better resolve the boundary layer and the unstructured mesh for the rest of the domain. The hybrid grid was chosen, instead of the structured grid only, to reduce the complexity of the mesh generation. Similar technique was employed in Refs. [2, 4, 13] and good agreements with the measurements were shown. The grid was divided into two zones, namely rotating and stationary zones (Fig. 1). These zones were linked via the sliding interface boundary condition. The rotating zone was generated at about one chord width bi-directionally from the blade surface resulting in an annulus-shaped zone. 500 nodes were distributed along the blade surface. The height of the first cell of the structured mesh adjacent to the blade was set to meet the value of the non-dimensional wall distance of $y^+ \approx 1$ in order to accurately capture the characteristics of the boundary layer. The y^+ is defined as u^*y/υ, where u^* is friction velocity, y is wall distance and υ is kinematic viscosity. This parameter is often used to describe how coarse or fine a mesh for a particular flow pattern. It is important in turbulence modeling to determine the proper size of the cells near domain walls. Because no wall function was employed in the present simulations; thus, according to Wang et al. [5, 6] and Buchner et al. [11] the y^+ for the RANS should be less than one to resolve the laminar sub-layer region ($y^+ \approx 5$). The maximum reported was around $y^+ \approx 5$ located near the trailing edge. The unstructured mesh was smoothed to reduce the skewness angle of the cells such that the maximum observed was less than 0.6. The relative distance of the turbine to both of the side walls was 8R. The inlet and outlet boundaries were located respectively 8R upstream and 24R downstream the turbine. The computational domains along with the boundary conditions used are presented in Fig. 1.

The Unsteady Reynolds averaged Navier Stokes (URANS) simulations have been conducted with a commercial CFD code, ANSYS Fluent 15.0. The two-equation eddy-viscosity *SST* k-ω turbulence model according to Menter [7] was employed. The model combines Wilcox k-ω [8] near the wall and standard k-ε model in the freestream. By doing so, accurate prediction of the flow field under a strong adverse pressure gradient can be given with small dependency towards the freestream conditions. This model was known to give good results for predicting separated flows [14]. Many computations for VAWTs have shown the accuracy of this model, for instance see Buchner et al. [11] and Orlandi et al. [13]. The intermittency transition model and the low Reynolds number correction were employed. The Kato-Launder correction [15] was applied to reduce the tendency of the RANS simulations to overpredict the turbulence production. This is particularly true for any simulation that employs a standard two-equation turbulence model. Having said that, the production limiter was activated to reduce the excessive turbulence kinetic energy in the stagnation regions. Coupled pressure-based solver was selected along with the second order implicit transient formulation. All solution variables were solved via the second order upwind discretization scheme.

3. CFD results

3.1 Static condition

This section presents the preliminary CFD results of the NACA 0012 airfoil simulations under static conditions using

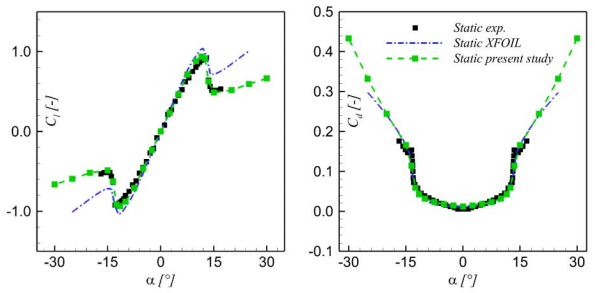

(a) (b)

Fig. 2. Static polar data. *Cl* (a); *Cd* (b).

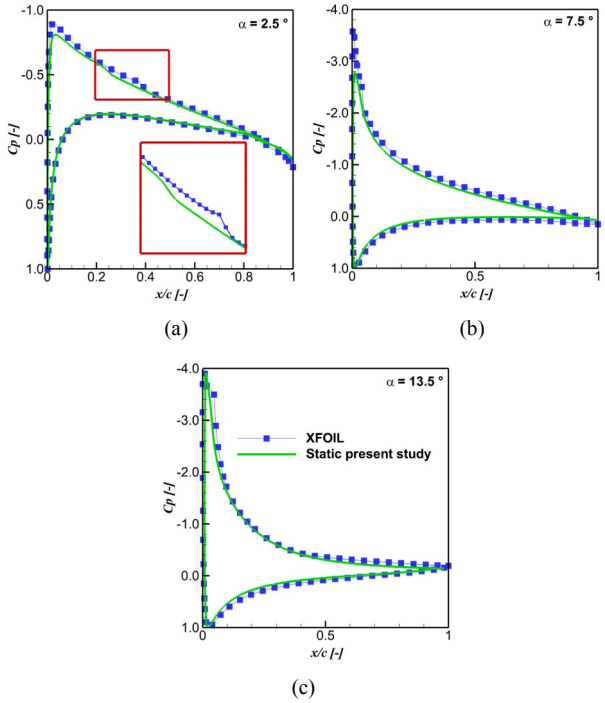

(a) (b)

(c)

Fig. 3. Static *Cp* distributions. $\alpha = 2.5°$ (a); $\alpha = 7.5°$ (b); $\alpha = 13.5°$ (c).

the same grid mesh as for the dynamic case displayed in Fig. 1.

The α was adjusted by rotating the rotating zone (red colored mesh in the enlarged area of Fig. 1) about the origin so that the desired α was obtained without giving too much changes on the grid domain. The Reynolds number was 1.35×10^5 calculated as $R_e = Uc/\upsilon$ with R_e, U, c and υ are Reynolds number, wind speed, chord length and kinematic viscosity, respectively. Steady calculations were performed for the linear lift region while unsteady calculations were carried out for $\alpha > 10°$. The static polar data, *Cl* and *Cd*, at several α are plotted against measurements from Lee and Gerontakos [16] as displayed in Fig. 2. Calculations using the boundary layer code XFOIL [17] are presented for comparison. It is observed that for $\alpha < 0°$, the polar data are reproduced by mirroring the results for the positive α.

A good agreement between the present study and the experiment is depicted in both lift and drag coefficients for the studied α range. The XFOIL calculations overpredict the lift coefficient at high α beyond stall. Generally, XFOIL shows a good agreement with the measurement for the linear region as also shown by Drela [17]. However, as α increases the boundary layer becomes thicker and the integral boundary layer methods, such as in XFOIL, are not recommended for such case. In addition, the transition model used can capture the drag bucket at $\alpha \approx 13.5°/-13.5°$. The predicted transition point is, however, a bit different from e^N model by XFOIL, see Fig. 3. The CFD simulation predicts earlier and less steep transition point than the one shown by XFOIL at $\alpha = 2.5°$, 7.5° and 13.5°. The difference is thought to originate from the inlet boundary condition specified in the CFD setup. The model is known to strongly dependent upon the inlet turbulence intensity and its dissipation rate. It shall be noted that the turbulence decays from the inlet to the location of the airfoil. The local value near the leading edge of the body is usually about half of the inlet [18]. It has been shown by Minkowycz et al. [19] that smaller turbulence intensity at the inlet results in a delayed transition location. The fact that CFD shows earlier transition location may indicate that the local turbulence level at the leading edge is higher. Hence, conscientious setup is necessary when dealing with these parameters. However, it should be noted that the described methods (in CFD and XFOIL) use different formulations and basis. This very fundamental difference may also have a significant contribution in the presented discrepancies. Nevertheless, the impact on the aerodynamic loadings is considerably minor as reflected from the XFOIL and the present study *Cl* and *Cd* which are less renounce in term of discrepancy for the examined α before stall.

3.2 Dynamic condition

The dynamic simulations were performed at similar inflow *Re* as in the static condition ($R_e = Uc/\upsilon$). The wind and the rotational (ω) speeds of the turbine were respectively 14 *m/s* and 46.67 rad/s which corresponds to the tip-speed ratio of $\lambda = 2$. The time step size used was 3.74×10^{-4} s, an equivalent to one degree blade revolution. The time step is calculated as $(2\pi/\omega)(\Delta\theta/360°)$, where $\Delta\theta$ (azimuth) is equal to 1°. Convergence is achieved every physical time step by setting the residual tolerance of all parameters to 1×10^{-5}, otherwise the calculation for the specific physical time is stopped after 200 iterations. The simulations were performed for 7 blade revolutions and the last three revolutions were extracted and averaged.

Fig. 4 shows the resulting non-dimensionalized forces in tangential (F_T) and normal (F_N) directions relative to the blade chord line. It can be seen that F_T is positive at certain azimuth ranges (zones 1, 2 and 3) implying negative power production which is defined as $P = -\omega R F_t$. Within zone 1, the negative power is caused dominantly by the drag force acting on the blade. The α seen by the blade within this range is considered small (Fig. 5) leaving F_T to strongly influenced by the drag force which is almost parallel to the direction of U.

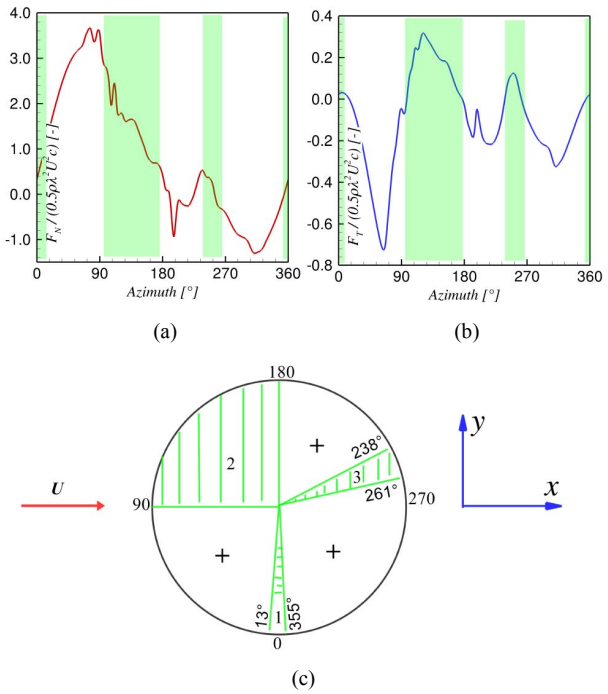

Fig. 4. Normal (a); tangential (b) forces acting on the blade. The shaded area (Zone 1,2 and 3) indicates the region where the resulting power production is negative (c). It should be noted that positive power production is obtained from negative tangential force.

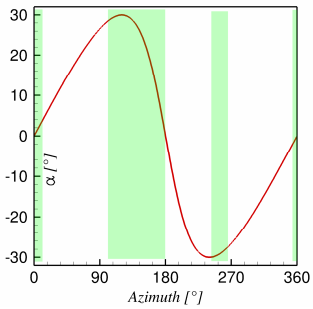

Fig. 5. Relation between azimuth angle and geometrical α.

For zone 2, the negative power production is strongly affected by flow separation on the blade suction side at high α which indicates the stall. The phenomenon starts at azimuth = 74° (α ≈ 22.9°). The flow insertion from the outside of the LEV pocket pushes the LEV to detach while the TEV grows stronger (Fig. 6). As the results, a sudden drop of F_N and a substantial increase of F_T are observed in Fig. 4. This effect occupies a wide azimuth range, from azimuth angle of 90° to 180°, in the turbine operation. In Fig. 6, distinct vorticity field upstream of the leading edge is observed which seems unphysical. This small error might be the results of non-smoothed transition between the structured and unstructured grids around that area. Another possibility comes from the block splitting issue where the interpolation within grid interfaces from one block to the neighboring blocks is not correctly made. This usually happens if the flow data need to be exchanged from the block consisting high velocity gradient information (with fine mesh) to the other blocks with lower velocity gradient (coarser mesh).

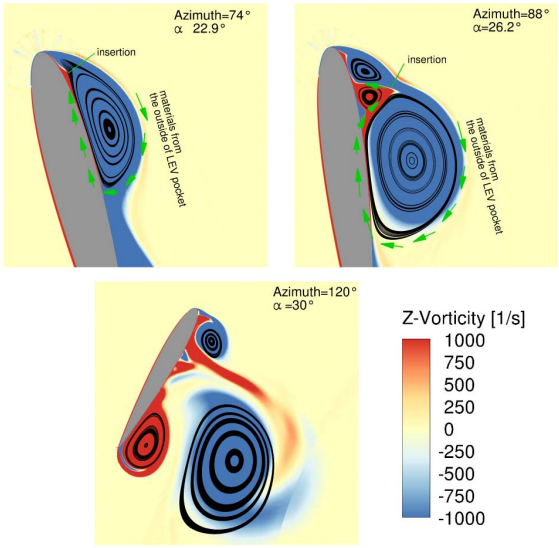

Fig. 6. Stall process by the flow insertion illustrated by *z*-vorticity, blue (CW) and red (CCW).

The negative power production in zone 3 is caused predominantly by the complex flow behavior occurring in the downwind phase. The BVI is identified as the main source of the power loss. It shows a strong influence from azimuth angle of 180° to 270°. To better understand the physical mechanism of such phenomenon, the flow development around the blade is illustrated in a series of snapshots in Fig. 7. The Clockwise (CW) vortex is indicated by the blue color while the Counter-clockwise (CCW) vortex is shown by the red color. The corresponding *Cp* distribution is plotted to get a better view on the impact of shedding vortices on the aerodynamic loading acting on the blade. The blade surface denoted by the letter "A" in each snapshot corresponds to the similar letter in the *Cp* distribution.

At azimuth 180°, five distinct vortices are observed, each labeled as *p*0, *p*1, *p*2, *p*3 and *p*4. The main vortex, *p*0, is the detached LEV from the blade surface, depicted earlier in Fig. 6, which travels alongside the blade and grows in size. This vortex deflects the main stream and determines the flow behavior close to the blade. All of the other vortices, namely *p*1 to *p*4, are at the same time encapsulated in a bigger vortex. The respecting vortex could also be seen as another *p*0 that deflects the mainstream hence inciting further power production loss. The vortex bundle is highly unstable and a strong interaction during the blade revolution is observed. The first vortex, *p*1, creates a strong blockage near the blade surface in the region pointed by the blue arrow. It accelerates the flow followed by the pressure decrease in the corresponding *Cp* plot. The stagnation point is not located on the leading edge, but is shifted downstream. The second vortex, *p*2, which rotates in opposite direction decelerates the flow downstream the minimum pressure region. The *p*3 vortex then increases the

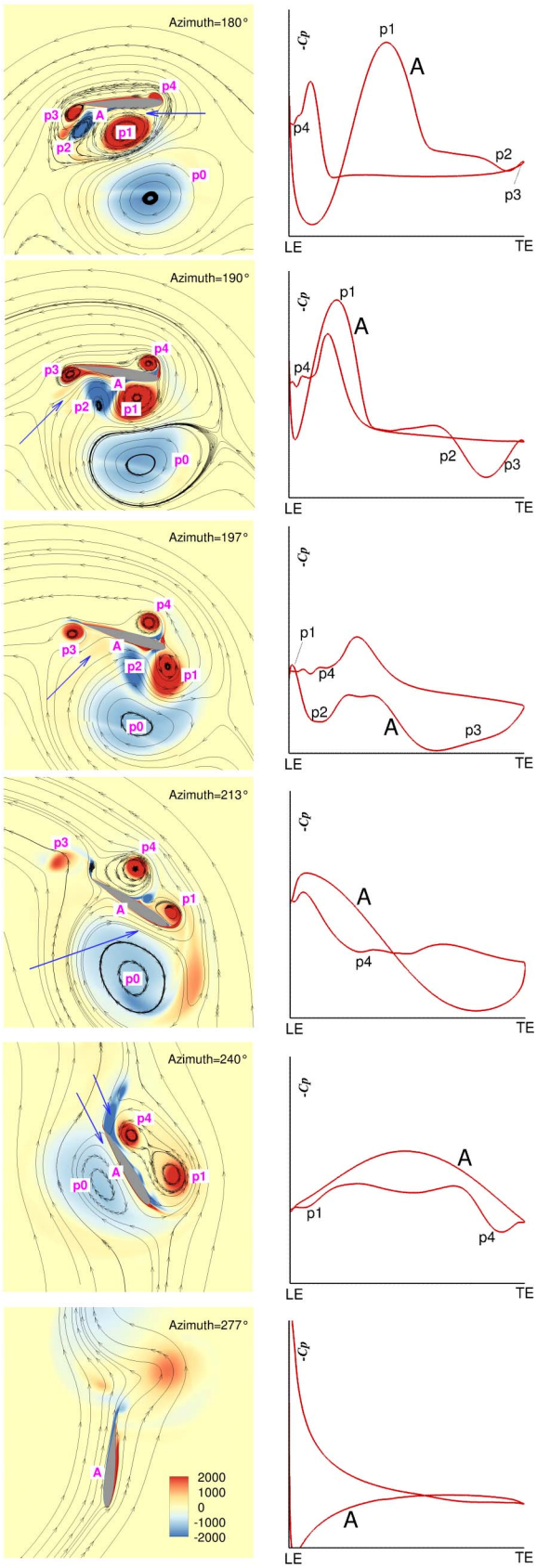

Fig. 7. BVI in the downwind phase illustrated by *z*-vorticity, blue (CW) and red (CCW), and the corresponding *Cp* distribution.

flow velocity in vicinity of the trailing edge. Meanwhile on the other blade side, *p*4 vortex has a very strong impact on the *Cp* distribution. No minimum pressure peak is observed as the incoming flow sees thicker structure than the actual blade structure itself due to the vortical structure existence. Downstream the vortex, the *Cp* distribution is flat similar with the flow over a flat plate.

At a larger azimuth angle, 190°, *p0* vortex still determines the flow behavior near the surface "A" creating a strong blockage on the mainstream. The *p*1 and *p*2 vortices travel towards the leading edge, shifting the location of the minimum *Cp* value further upstream. A substantial pressure increase close to the trailing edge is also observed. This happens because the flow between the *p*2 and *p*3 vortices is nearly orthogonal to the blade, see the blue arrow in Fig. 7 at azimuth 190°. Similarly on the other blade side, the strength of the *p*4 vortex is also increasing making the affected region wider.

As observed, F_N and F_T are decreasing from azimuth angle of 180° to 190°. It is caused mainly by the pressure change on the surface "A" of the blade which is generally increasing. A further increase of azimuth angle, at 197°, an abrupt decrease/increase of the normal/tangential force is observed. The *Cp* distribution which generates these forces is shown in Fig. 7. It can be seen that the surface "A" of the blade has a substantially higher pressure than on the opposite surface. Hence, it is obvious that F_N is decreasing. There is a region in the front and the rear sides of the blade where the pressure is very high due to the *p*2 vortex and the orthogonal flow (blue arrow) as discussed for azimuth = 180°. It is identified as the source of the substantial F_T increase depicted in Fig. 4. However, the resulting F_T increase is lower than zero so that the power production is still positive. In addition, the shape of the *p*0 vortex changes and it moves closer to the *p*1 and *p*2 vortices. This phenomenon, nevertheless, occurs only within a narrow azimuth range.

The *p*0 and *p2* vortices which have the same direction merge and create a larger vortex at azimuth = 213°. The newly generated vortex increases the backflow velocity on the front side of the blade (see the blue arrow) which leads to *Cp* decrease. On the other hand, the *p*1 vortex which strongly influence the surface "A" of the blade at lower azimuth angles is transported towards the opposite blade surface. Shortly before it is convected downstream, the vortex detaches from the blade surface and it interacts with the *p*4 vortex at azimuth = 240°. Additionally, the *p*0 vortex becomes very close to the blade surface. These all vortices (*p0*, *p*1 and *p*4) change of the flow direction close to the blade surface, see the blue arrows. This results in a higher pressure level on the blade rear side leading to F_T increase. The surface "A" of the blade also shows lower *Cp* than the other blade surface resulting in an increase of F_N. These interacting vortices shed away with further increase of the azimuth angle. It can be seen that the flow is fully re-attaching on the blade at azimuth = 277°.

Though the BVI is complex and demonstrated to strongly influence the blade loads, the phenomenon gives a small im-

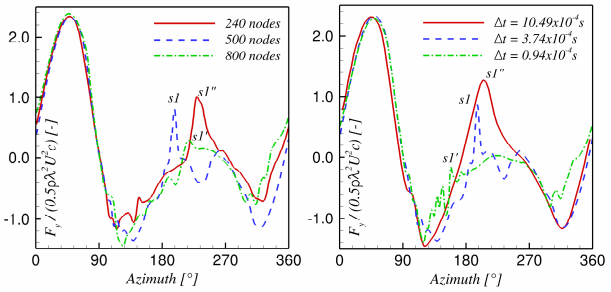

(a) (b)

Fig. 8. Force acting on the blade in *y*-direction: (a) Effects of grid density; (b) time step size used.

pact on the power production loss. It covers only 6.4 % of the azimuth range where the turbine produces a negative power. This is considered small compared to the dynamic stall impact within zone 3 which covers almost 22 %.

It has been shown that the VAWT performance is strongly influenced by the DS phenomenon. It is shall be noted also that the assumption of rigid surface may lead to a different conclusion when the surface deformation occurs [21]. Thus, an accurate but efficient prediction of the DS is important which can be done by adjusting the turbulence model for the DS purpose [23]. At last, separation needs to be controlled [24] to fully optimize the VAWT under realistic conditions.

3.3 Grid and time resolutions

In this section, the impacts of spatial and temporal discretizations on the resulting aerodynamic loading for the dynamic case are investigated. For the spatial discretization study, the grid along the blade surface was refined from 500 nodes (baseline) to 800 nodes. A coarser grid of 240 nodes along the blade was also tested. No specific criteria are used, but the grid refinement should be at least by a factor of 1.4 according to the grid convergence index study introduced by Celik et al. [20]. This approach was also tested in Ref. [21] for applications in HAWT blade. Simulations for the grid study were performed using the same time step size as the baseline case (1°). The temporal discretization study was conducted by coarsening and refining the baseline time step size ($3.74\text{x}10^{-4}$ *s*) by a factor of 4 using the same mesh as the baseline case (500 nodes). The fine time step size is $0.94\text{x}10^{-4}$ *s* (0.25°) and the coarse time step size is $10.49\text{x}10^{-4}$ *s* (4°).

The results in term of the non-dimensionalized force in *y*-direction (F_y) are plotted in Fig. 8. In both studies, the refinements have small impact within the azimuth range of 0° to 109°. The discrepancy is, however, quite pronounced for the rest of azimuth angles. A distinct peak of F_y (*s*1) for the baseline case is observed at azimuth 197°. It is predicted at a slightly higher azimuth angle for the fine grid resolution and significantly higher angle for coarse mesh. The peak value reduces with increasing resolutions of both grid and time step. This implies that the physical impact of the flow at azimuth =197° is a little bit over-predicted. It is predicted at a smaller azimuth angle with increasing time step size resolution.

Generally, finer grid and time resolutions produce more accurate results than the coarser one, but it is followed by computational time increase as a consequence. For RANS simulations, as the turbulence is not resolved (but modeled), grid and time-step refinements will reach a converged solution at a certain value. It can be seen from Fig. 8 that the general behavior and characteristics of the resulting force are sufficiently captured using the baseline grid and time step size. Furthermore, the same grid was used to calculate the static airfoil case presented in Sec. 3.1 and excellent agreements are achieved against measurement data. Thus, considering the solution accuracy and computational resources, the use of baseline grid and time is reasonable.

4. Conclusion

Computational fluid dynamics (CFD) simulations have been carried out to study a single bladed Vertical axis wind turbine (VAWT) under stalled conditions at low tip speed ratio (λ=2). The studied turbine blade was constructed using the NACA 0012 airfoil. The Blade vortex interaction (BVI) was investigated and highlighted as the main focus of this paper.

For the preliminary study, calculations were carried out for the NACA 0012 airfoil under static condition. The results were compared with the measurement data obtained from literature and simulations using a boundary layer code XFOIL. A good agreement was obtained in lift and drag coefficients. The present simulations were able to capture the deep stall in lift and the drag bucket accurately. Although the transition point was predicted a bit earlier for the CFD prediction than the XFOIL code, the resulting forces are similar before stall implying that the impact is minor.

Under dynamic conditions, the resulting tangential force was positive at certain azimuth ranges implying negative power generation. Three different ranges and the causes of this phenomenon were depicted as follows:

- Zone 1 covered a very small azimuth range. The positive tangential force was caused mainly by the drag and the angle of attack (α) was considered small.
- Zone 2 covered a large portion of azimuth range. Flow separation at large α caused dynamic stall and became the main reason of the power loss.
- Zone 3 covered a mediocre portion of azimuth range. The BVI occurring within this range strongly influenced the flow characteristics associated with the power loss. Five distinct vortices, *p*0, *p*1, *p*2, *p*3 and *p*4 were involved in this phenomenon. A very strong influence of these interacting vortices on the pressure coefficient (*Cp*) distribution was demonstrated. The flow behavior was determined by the blockage created by the *p*0 vortex. The other vortices, namely *p*1 to *p*4, at the same time encapsulated in a bigger vortex which could be seen as another *p*0 that deflects the mainstream hence inciting fur-

ther power production loss.

The spatial and temporal discretization studies showed that the finer grid/time resolution had small impact on the blade load for the attached flow at small azimuth angles. At azimuth > 109°, larger discrepancies were observed. Nevertheless, the general behavior of the resulting force was sufficiently captured using the baseline grid and time step size.

Acknowledgment

This work was supported by the Ministry of Research, Technology and Higher Education of Indonesia through the Directorate General of Higher Education (DGHE) scholarship.

References

[1] J. Svorcan, S. Stupar, D. Komarov, O. Peković and I. Kostić, Aerodynamic design and analysis of a small-scale vertical axis wind turbine, *Journal of Mechanical Science and Technology*, 27 (8) (2013) 2367-2373.

[2] N. Qin, R. Howell, N. Durrani, K. Hamada and T. Smith, Unsteady flow simulation and dynamic stall behaviour of vertical axis wind turbine blades, *Wind Engineering*, 35 (4) (2011) 511-510.

[3] F. Scheurich, T. M. Fletcher and R. E. Brown, Simulating the aerodynamic performance and wake dynamics of a vertical-axis wind turbine, *Wind Energy*, 14 (2) (2011) 159-177.

[4] G. Hutomo, G. Bangga and H. Sasongko, CFD studies of the dynamic stall characteristics on a rotating airfoil, *Applied Mechanics and Materials*, 836 (2016) 109-114.

[5] S. Wang, D. B. Ingham, L. Ma, M. Pourkashanian and Z. Tao, Turbulence modeling of deep dynamic stall at relatively low Reynolds number, *Journal of Fluid and Structures*, 33 (2012) 191-209.

[6] S. Wang, D. B. Ingham, L. Ma, M. Pourkashanian and Z. Tao, Numerical investigations on dynamic stall of low Reynolds number flow around oscillating airfoils, *Computers and Fluids*, 39 (2010) 1529-1541.

[7] F. R. Menter, Two-equation eddy-viscosity turbulence models for engineering applications, *AIAA Journal*, 32 (8) (1994) 1598-1605.

[8] D. C. Wilcox, *Turbulence modeling for CFD* 2, La Canada, CA, DCW industries (1998).

[9] G. Bangga and H. Sasongko, Numerical investigation of dynamic stall for non-stationary two-dimensional blade airfoils, *Proc. of the Annual Thermofluid Conference 4*, Yogyakarta, Indonesia (2012).

[10] G. Bangga, Assessment of Modified Two-Equations URANS Turbulence Model to Predict the Onset of Dynamic Stall, *M.Sc. Thesis*, Mechanical Engineering Department, Institut Teknologi Sepuluh Nopember, Surabaya, Indonesia (2013).

[11] A. Buchner, M. Lohry, L. Martinelli, J. Soria and A. J. Smits, Dynamic stall in vertical axis wind turbines: Comparing experiments and computations, *Journal of Wind Engineering and Industrial Aerodynamics*, 146 (2015) 163-171.

[12] C. Ferreira, The Near Wake of the VAWT, 2D and 3D Views of the VAWT Aerodynamics, *M.Sc. Thesis*, Aerospace Engineering Department, TU Delft, The Netherlands (2007).

[13] A. Orlandi, M. Collu, S. Zanforlin and A. Shires, 3D URANS analysis of a vertical axis wind turbine in skewed flows, *Journal of Wind Engineering and Industrial Aerodynamics*, 147 (2015) 77-84.

[14] B. Kim, W. Kim, S. Bae, J. Park and M. Kim, Aerodynamic design and performance analysis of multi-MW class wind turbine blade, *Journal of Mechanical Science and Technology*, 25 (8) (2011) 1995-2002.

[15] M. Kato and B. E. Launder, The modeling of turbulent flow around stationary and vibrating square cylinders, *Proc. 9th Symposium on Turbulent Shear Flows*, Kyoto, Japan (1993) 10.4.1-10.4.6.

[16] T. Lee and P. Gerontakos, Investigation of Flow over an Oscillating Airfoil, *Journal of Fluid Mechanics*, 512 (2004) 313-341.

[17] M. Drela, XFOIL: An analysis and design system for low Reynolds number airfoils, *Low Reynolds Number Aerodynamics*, Springer Berlin Heidelberg (1989) 1-12.

[18] R. Langtry and F. Menter, Transition modeling for general CFD applications in aeronautics, *AIAA Paper 522.2005* (2005) 14.

[19] W. Minkowycz, J. Abraham and E. Sparrow, Numerical simulation of laminar breakdown and subsequent intermittent and turbulent flow in parallel-plate channels: Effects of inlet velocity profile and turbulence intensity, *International Journal of Heat and Mass Transfer,* 52 (17) (2009) 4040-4046.

[20] I. Celik, U. Ghia, P. Roache, C. Feritas, H. Coleman and P. Raad, Procedure for estimation and reporting of uncertainty due to discretization in CFD applications, *Journal of Fluids Engineering,* 130 (2008).

[21] G. Bangga, T. Lutz and E. Krämer, An examination of rotational effects on large wind turbine blades, *Proc. of the EAWE PhD Seminar 11*, Stuttgart, Germany (2015).

[22] A. Heydari and M. Pasandideh-Fard, Lift characteristics of pitching NACA0015 airfoil due to unsteady forced surface inflation, *Journal of Mechanical Science and Technology*, 29 (6) (2015) 2365-2373.

[23] G. Bangga and H. Sasongko, Dynamic stall prediction of a pitching airfoil using an adjusted two-equation URANS turbulence model, *Journal of Applied Fluid Mechanics*, 10 (1) (2017).

[24] H. Shim and S.-O. Park, Passive control of pitch-break of a BWB UCAV model using vortex generator, *Journal of Mechanical Science and Technology*, 29 (3) (2015) 1103-1109.

Galih Bangga is currently working as a Researcher at the Institute of Aerodynamics and Gas Dynamics, University of Stuttgart, Germany. His research interests include wind turbine aerodynamics, flow separation and airfoil design.